Aerodynamic Shape Optimization of UAV Fuselage and Fairings with Payload Integration

Luís Dias Pinheiro luis.pinheiro@tecnico.ulisboa.pt

Instituto Superior Técnico, Universidade de Lisboa, Portugal July 2025

Abstract

The usage of powerful optimization tools is becoming common in solving many engineering problems due to available computational resources and mature numerical algorithms. In this work, an adjointbased high-fidelity aerodynamic shape optimization framework is used to manipulate a generic aircraft fuselage shape to minimize the total aerodynamic drag with specific payload volume constraints. The external fuselage shape is modified using the free-form deformation (FFD) technique to allow greater flexibility. The impact of using different deformation approaches applied to the displacement of FFD control points is studied, including displacements along the normal direction, the transverse axis directions, and cambering along the fuselage longitudinal direction. It is demonstrated that the combination of flexible control point displacement in multiple FFD box cross-section planes together with a streamwise cambering can produce a very significant drag reduction, in excess of 40% compared to the selected baseline shape, while still satisfying volume constraints to account for internal or protruding payloads. Additionally, to complement the study, two real case scenarios inspired by TEKEVER UAV projects are tackled, representing realistic integration challenges within UAV fuselages. The first case handles the integration of a SATCOM antenna, represented by its enclosing spherical volume, while the second case deals with the integration of a recovery parachute system, represented by an inclined box. The final optimization cases highlighted the potential for aerodynamic improvement, with Case 1 achieving a 4.6% drag reduction driven by lower pressure drag, while the last case demonstrated a 25% drag increase due to stricter constraints and abrupt fuselage expansion.

Keywords: aircraft design, gradient-based optimization, adjoint method, free form deformation, high-fidelity analysis, aerodynamic performance

1. Introduction

In recent years, the aviation industry has been expanding towards more diverse solutions, proposing novel aircraft configurations and shapes. In particular, Unmanned Aerial Vehicles (UAVs) have become increasingly relevant in multiple sectors, including agriculture, defense, and civil operations [1, 2]. With the market expanding in the UAVs, fuselage shape optimization becomes imperative to enhance the aerodynamic efficiency, structural attachment, and overall performance.

The study focuses on the aerodynamic shape optimization of a typical fuselage using gradient-based strategies to obtain a fast convergence towards an optimal design. The gradients of the objective and constraint functions are calculated using the adjoint method [3], allowing the computational cost to remain independent of the number of design variables, which is particularly beneficial in shape optimization problems.

The Free-Form Deformation (FFD) method [4] is

used to parameterize the fuselage geometry to allow flexible and smooth shape changes. The deformation strategy includes displacements along the longitudinal axis and normal-based deformations of the control points, as well as local shape adjustments in critical regions such as the nose and tail.

To complement the baseline study, two case scenarios inspired by TEKEVER UAV projects are introduced. These aim to replicate real-world integration challenges by imposing internal constraints: a spherical volume representing a SATCOM antenna, and an inclined box simulating a parachute installation. These geometries pose local constraints in the fuselage which must be maintained throughout the optimization process, giving further insight into the enforcement of constraints and control of shape in real-world applications. In order to guarantee design feasibility, these volume constraints are applied to preserve payload capacity and ensure that the resulting fuselage geometries remain suitable for internal component allocation and structural inte-

gration. Through this framework, this work investigates the potential of shape optimization techniques to generate efficient, realistic, and mission-oriented fuselage designs.

2. Background

2.1. Aerodynamic Forces

An aircraft's aerodynamic performance is essentially determined by the forces developed upon its interaction with the surrounding airflow. These forces are caused by the pressure and shear stress distribution along the body surface and give rise to lift and drag components. Among these, drag is a dominant factor in aircraft design since it influences fuel economy, range, and cost of operating the aircraft. Aircraft shape optimization, and most particularly fuselage, is therefore mainly directed at minimizing drag [5].

Generally speaking, the drag is usually divided into three different categories, 1) Parasitic drag consisting of form drag, skin friction, and interference drag; 2) Lift-induced drag; and 3) Wave drag. In this work, the main focus was on the first category, since the wave drag [6] is important only for transonic and supersonic speed, and the lift-induced drag is created due to the lift, and fuselages are not known for the generation of lift [7].

Among the components of parasitic drag, interference drag occurs at component intersections as a result of boundary layer distortion and secondary flows. Since no component intersections are taken into account in the optimization problems, the attention is focused on skin-friction and form drag [5].

Consequently, the optimization process targets minimizing the remaining two types. Skin-friction drag arises from boundary layer shear stresses and depends on the surface area and flow regime. Although typically smaller than form drag, it becomes increasingly significant when optimal geometries with higher surface areas, like fuselages integrating the payload, are being optimized. Another important type of drag, the form drag, also referred as pressure drag, is the drag on a body moving through a fluid due to the pressure difference between the front and rear of the body. This type of drag is directly dependent on the shape, or "form", of the body, and is most pronounced when there is flow separation. When the shape is poorly streamlined, the flow is not capable of remaining attached to the surface and is separated from the surface, creating a wake area that is a region of low pressure with increased turbulence. The larger and more chaotic this wake, the greater the pressure difference between the front and rear regions of the fuselage [8].

2.2. Computational Fluid Dynamics (CFD)

Computational fluid dynamics (CFD) is a fundamental tool used to simulate turbulent flows in aerospace applications. Unlike experimental means, CFD provides a cheaper and more flexible ways of simulating complex flows, especially around components like fuselages and wings.

The simulations done in this work are based on the Navier–Stokes equations, which dictate the conservation of energy, mass, and momentum in fluid flow and are the basis of CFD. Because of the increased computational cost of simulating all of the scales of turbulence with DNS or LES, a Reynolds-Averaged Navier–Stokes (RANS) strategy was used. RANS, on the other hand, offers time-averaged solutions for the flow, which is an effective and affordable way to simulate turbulent flows in engineering applications. Note that this method introduces additional terms that account for the effects of turbulence, increasing the number of variables [9].

To solve this problem, a turbulence model is required. For this work, the Spalart–Allmaras (SA) was chosen. This is one of the most widely used method in aerospace applications [10]. It is one of the most straightforward, yet efficient method for simulating turbulent flows.

Additionally, since the selected CFD solver only provides a differentiated version of the Spalart-Allmaras turbulence model, and gradient-based optimization will be used, this decision becomes essential for our research [11].

2.3. Optimization Methods

Computational design problems are becoming more common in manufacturing industries. For complex systems like UAVs, the design is one of the most important characteristics to take into consideration. Optimizing to the specified objectives functions can lead to several improvements. It is an engineers' job to formulate the correct problem and find the desired parameters according to the objectives. In mathematical language, the optimization task can be posed as

$$\begin{array}{lll} \text{Minimize} & f(x) \\ \text{by varying} & x_i & i = 1, \dots, n_x \\ \text{subject to} & g_j(x) \leq 0 & j = 1, \dots, n_g, \\ & h_l(x) = 0 & l = 1, \dots, n_h, \\ & \underline{x}_i \leq x_i \leq \overline{x}_i & i = 1, \dots, n_x. \end{array} \tag{1}$$

and it basically demonstrates how an optimization problem works: by adjusting the design variables x_i within the boundaries of the constraints g_j and h_l , the objective function f can be minimized [12].

Gradient-based methods were selected in this

work because they are efficient and deterministic, meaning they follow a defined sequence and return consistent results. These algorithms depend on derivative information to drive the optimization process and are best suited to problems with a large design variable list.

To solve the constrained, nonlinear optimization problems defined throughout this work, the Sequential Least Squares Quadratic Programming (SLSQP) algorithm was used. SLSQP iteratively solves quadratic approximations to the Lagrangian, while linearizing the constraints, with the benefit of robustness as well as efficiency. Its stability and documented performance in aerospace applications made it a suitable option for the current optimization framework [13].

After selecting the optimization algorithm, it is important to select a suitable algorithm to effectively compute the derivatives based on the problem dimension. In this work, the chosen method was the adjoint method. The adjoint method is considered to be an efficient and accurate method to evaluate the sensitivities of a cost function. Its key advantages is that its computational cost remains independent of the number of design variables [3].

3. Implementation

This work uses the MACH-Aero framework to carry out aerodynamic shape optimization [14]. This framework combines various tools to deform the geometry, generate high-quality meshes, execute CFD simulations, and iteratively update the design in accordance with the specified variables and constraints.

The fuselages are parameterized using pyGeo, which maps the surface mesh of the geometry to a block of control points defined by the Free-Form Deformation (FFD) box [4]. Once the surface deformation is defined, it is propagated to the volume mesh using IDWarp [15], a MACH-Aero meshwarping tool that preserves mesh quality through an inverse distance weighting algorithm.

During the pre-processing stage, the initial mesh is generated through pyHyp, a hyperbolic mesh generation tool that employs a marching algorithm to create high-quality structured grids for CFD simulations. ADflow is the computational fluid dynamics (CFD) solver responsible for analysing the aerodynamic performance of each candidate geometry [11]. The Reynolds-Averaged Navier–Stokes equations are solved using the Spalart–Allmaras turbulence model.

Finally, PyOptSparse [16] is an object-oriented framework for formulating and solving nonlinear constrained optimization problems. It coordinates the design variable updates, uses gradient information provided by pyGeo and ADflow, and drives the

iterative process towards an optimal solution.

Collectively, these tools support fast optimization cycles, keep mesh quality intact, and allow effective handling of intricate geometries.

As mentioned, the FFD method serves as the parametrization approach in this work, and it is employed using tools from the open-source MACH-Aero optimization framework. This method is a geometry modification technique that parametrizes the shape perturbation instead of the shape itself [4]. It works as a control structure that encloses the embedded fuselage, and any displacement applied to its control points results in a smooth deformation of the volume inside. Note that the nodes that are moved are located on the outer surface of the FFD box and are referred to as FFD control points. These nodes are mathematically linked to the mesh points inside the box. When the control points suffer any displacement, all the points within the FFD box, including those on the fuselage surface, are automatically deformed based on their position relative to the box. By using the FFD method, the geometry of the object is embedded into a box that can be manipulated by moving these outer control nodes, allowing for smooth and continuous shape changes.

Another primary operation of the aerodynamic optimization approach that has direct impact on CFD accuracy as well as the computational cost of simulations is the mesh generation [17]. Surface mesh forms the outer boundary of the computational domain and provides an initial point to create a volume mesh. For this purpose, structured surface meshes were generated from the fuselage CAD geometry (Fig. 1) using a multi-block topology.



Figure 1: Complete CAD model of the TEKEVER ARX drone

Once the surface mesh was defined, the volume mesh was generated using pyHyp. It starts with a surface corresponding to the geometry, in this case, of the TEKEVER ARX or the mesh used for the parametrization studies; and then extrudes the mesh in successive layers until it reaches the defined distance from the original surface, forming a structured volume mesh suitable for high-fidelity CFD analysis. Several parameters were necessary to be defined to complete this task. These include the first-layer height (s0), the number of lay-

ers to extrude (N), and the total marching distance (marchDist), for example. Besides these, more parameters are available to change the algorithm that generates the mesh. However, default values were used, as they seemed appropriate to generate the fuselage due to their previous integration in similar shape optimization problems. Furthermore, the computational domain was extended in the streamwise direction up to five chord lengths behind the fuselage and the surface was extruded in all outward directions to generate the full volume mesh around the fuselage to ensure sufficient space for flow development and ensure proper resolution of the wake and pressure recovery region.

Note that for more complex geometries like the TEKEVER ARX, an overset approach is applied. Instead of having one complex mesh, this method allows to split the domain into separate and overlapping meshes. The information of these meshes is then interpolated in each iteration [18]. This process helps generating meshes with refined regions, such as near the trailing and leading edge of the fuselage.

4. Results

The initial goal was to understand how different FFD control point parametrization approaches could be applied to a generalized fuselage geometry. Each approach was evaluated individually to assess its influence on the final shape, guiding the selection of the most suitable approach for the final optimization studies. The explored approaches included normal-based and axis-oriented displacements. In addition, a method for introducing camber into the fuselage was also implemented. These deformation strategies were first tested separately and then combined to start integrating payload constraints, in specific, a spherical volume intersecting the fuselage surface was introduced. The objective was to evaluate how the optimizer would reshape the fuselage around the sphere, resulting in a deformed geometry that accommodates the payload while preserving aerodynamic performance.

An example of a comparison between the baseline fuselage (in black) and the optimal one (in red) can be observed in Fig.2. In this study, the goal was to enclose the sphere that was initially intersecting the baseline fuselage. This was achieved by allowing displacements along the Z-axis in the y=0 plane, combined with normal-based displacements for the rest of the FFD box. This led to, as summarized in Tab.1, a 21.3% decrease in overall drag mainly due to volume and area minimization. Since no constraints were imposed, the fuselage would be expected to shrink even more, but the imposed lower bounds of the design variables did not allow this to happen.

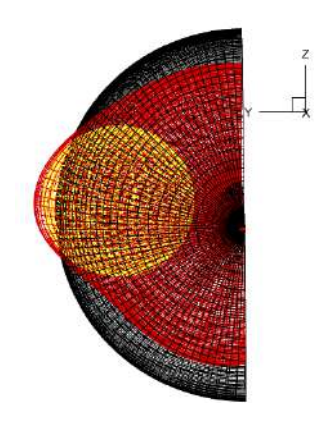


Figure 2: Parametrization along Z-axis, combined with normal vectors of FFD points.

Table 1: Optimization deformation strategy studies and corresponding drag coefficient reduction.

Approaches	Constraints	ΔC_D
(baseline)	_	ref
Normals	None	-16.6%
Y-axis	None	-21.6%
Z-axis	None	-11.7%
(Y, Z)-axis	None	-40.4%
Nose Camber	None	-2.1%
Tail Camber	None	-2.1%
(Tail, Nose) Camber	None	-2.3%
Camber + Normals	None	-17.1%
Camber $+ (Y, Z)$ -axis	None	-41.6%
Camber + Normals	TS (IS)	-16.9%
Camber $+ (Y, Z)$ -axis	TS (IS)	-39.8%
Normals	TS (IS)	-16.4%
Normals	TS (IntS)	-7.0%
Normals + Z-axis	TS (IntS)	-21.3%

TS = Triangulated Surface, IS = Internal Sphere,

IntS = Intersected Sphere.

Through the analysis of the optimal shapes presented, corresponding to the cases stated in Tab. 1, it was possible to asses the effectiveness of the different shape parametrization approaches. Notice, however, that these optimal shapes were obtained from problems that differed slightly in terms of design variable bounds to overcome mesh morphing fails. As such, the comparisons might not extrapolate directly to other fuselage geometries.

Looking at the approaches using deformations along the Y- and Z-directions, they exhibited a much greater drag reduction compared to the normal direction approach. The Y-direction only approach, corresponding to lateral fuselage deformations, led to considerably better shapes compared to the Z-direction only approach, and, unsurprisingly given the greater deformation freedom, the combination of both Y- and Z-direction deformations led to an impressive 40% drag reduction. Even though

this parametrization approach allowed the largest minimization of drag, it still had some irregularities that had to be taken into account.

When considering the deformation using the camber function alone, little impact in the aerodynamic performance was obtained, limited to about 2% reduction in drag, regardless of the regions manipulated (nose, tail or both).

Referring to the cases where the payload was intersected with the fuselage surface, the last two approaches presented in Tab. 1, only the deformation strategy along the normal vectors was considered because it prevented irregular deformations in the fuselage while integrating the triangulated surface constraint with the sphere intersected in the main body. However, when comparing these cases, the case where only displacements along the normals of the FFD points were considered, resulted in a 7% drag reduction, while the combination with Z-direction displacement in the plane y=0 significantly increased the reduction to over 21%, mostly due to the influence of manipulating the FFD points near the fuselage's vertical symmetry XZ-plane.

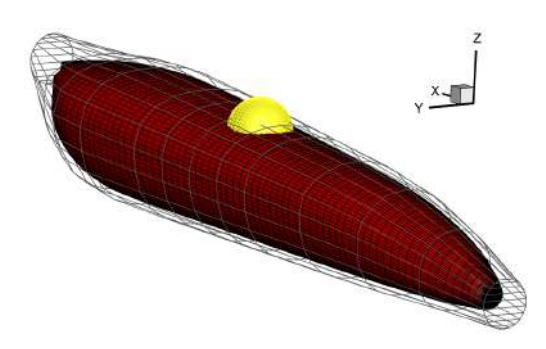
Overall, for these cases, a drag reduction ranging from 2.1% to 41.6% was observed. Despite the directional parametrization leading to greater drag reduction, the parametrization along the normal vectors of the FFD box points was not discarded in the TEKEVER ARX study cases. This approach combined with a deformation along the vertical Z-axis in the y=0 plane have produced good results as well, with the added benefit of reducing the surface irregularities if the DV bounds are properly set. This study highlighted the importance of selecting appropriate parametrization approaches based on both aerodynamic performance and payload constraints (internal to the fuselage or partially protruding).

To further enhance the research, the already tested parametrization approaches were implemented to the TEKEVER ARX fuselage, which has a more complex and realistic shape shown in Fig. 1. In relation to the original generic studies, a number of modifications were required to obtain efficient and effective results.

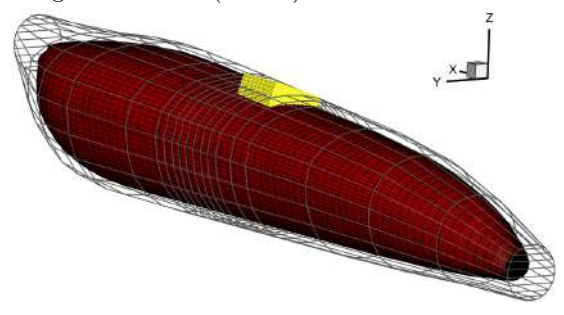
In the end, four cases were examined. However, since the third case was a combination and improvement of the first two cases, these were not documented here.

The third case represented an integration of a spherical volume that intersects the fuselage skin, simulating a volume that fully encloses a SATCOM antenna, observed in Fig. 3a. The integration process experienced a number of problems, including mesh failures, lack of symmetry of the obtained results, despite the problem's symmetry, and extended computation time due to the slow conver-

gence of the residuals. The fourth case, shown in Fig. 3b, aimed to integrate an inclined box modeling the installation of a parachute system. The presence of sharp corners and edges of the box caused frequent mesh generation problems and convergence issues as well.



(a) TEKEVER ARX fuselage optimisation with an integrated satcom (Case 3).



(b) TEKEVER ARX fuselage optimisation with an integrated parachute (Case 4).

Figure 3: Comparison between two TEKEVER ARX fuselage optimisation cases.

After trying the various deformation approaches, it was found that displacements along the fuselage's Y and Z axes were the most suitable to achieve the shape changes required in each case. To reduce the computational cost, an approach to deform only half of the FFD box was adopted by inserting a symmetry plane at y = 0. by pairing the FFD box control points on opposite sides of the symmetry plane. This decreased the number of design variables and increased overall optimization efficiency. Another problem encountered while optimizing these four cases was the fact that the optimizer often got trapped preventing further progress when the fuselage surface intersected the sphere or box surfaces. To overcome this, a modified baseline fuselage was generated to ensure the entire box was enclosed. This was achieved by applying a vertical translation to selected FFD nodes along the Z axis, effectively lifting the FFD box and, consequently, the fuselage. The resulting geometry served as the new initial shape for the optimization problem. An example of this issue is shown in Fig. 4 where a comparison between the initial baseline fuselage (black)

and the optimized result (red) is made.



Figure 4: Comparison between the baseline fuselage (Black) and the optimized result (Red) (case 4).

Particularly, in the fourth case, even though the optimizer could still converge under these conditions, it did not satisfy all the constraints due to the presence of sharp corners and edges in the original box design. These sharp edges and corners restricted the ability of the optimizer to create a continuous, smooth surface around the reference shape. Consequently, additional changes to the box were made and therefore, all sharp edges and corners were eliminated. This modification minimized conflicting constraints and facilitated the optimizer's ability to identify feasible solutions that better integrated the box within the overall fuselage shape.

Although the same mesh was used in both optimization cases, the FFD box configurations were quite different, see Figs. 3a and 3b. The third case provided the optimizer with far greater freedom, with a greater number of FFD control points allowed to move. As shown in Tab. 2, while the number of design variables did not differ significantly between the two cases, the control points of the third case were spaced further apart. This means that each displacement influenced a larger area of the fuselage, causing a larger shape modification.

In contrast, the fourth case needed tighter geometric control, as it aimed to integrate an inclined box that modeled a parachute system without deforming the front part of the fuselage. The FFD control points were placed closer to the payload, aiming to achieve a localized deformation around the inclined geometry. To manage this integration more precisely, a new FFD box was defined with additional sectional divisions near the payload. The nodes near the front of the box were kept fixed, preventing the optimizer from modifying the geometry in that region, while the other selected nodes were allowed to move along the Y and Z axes.

The bounds imposed on the FFD control points also differed between the two cases, as the payloads were located in distinct regions of the fuselage. Furthermore, in the fourth case, the objective function had to be scaled down to ensure smoother displacements. This adjustment was necessary since, as explained, whenever the two surfaces intersected, the optimizer would get trapped leading to a failed op-

timization.

In general, each case presented distinct challenges related to FFD box design, control point placement, and optimization parameters. These constraints led to different outcomes, which will be analysed in detail. A comparison of the optimization setups will be provided, followed by an analysis of the pressure coefficient (C_p) and skin friction coefficient (C_f) distributions for both cases.

The parameters used for this third case (case 3) are summarized in Tab. 2. The triangulated surface constraint was applied with a spatial tolerance of $\rho=750$, to promote better spatial fitting between the deformed fuselage and the SATCOM sphere. Overall, this setup was designed to improve convergence behaviour and explore if symmetry and improved enforcement of spatial constraint could lead to more efficient fuselage shapes.

A detailed comparison between the baseline and optimized fuse lages for case 3 are presented through the pressure and skin-friction coefficient distributions, shown in Figs. 5 and 6, with the baseline fuse lage on the left side and the optimized geometry on the right side in each figure. The different views are divided along the symmetry plane at y=0, providing a clear comparison of the two coefficients between the two stages of the optimization. The following analysis highlights the key differences between the two configurations and examines the aerodynamic implications of the applied surface deformations.

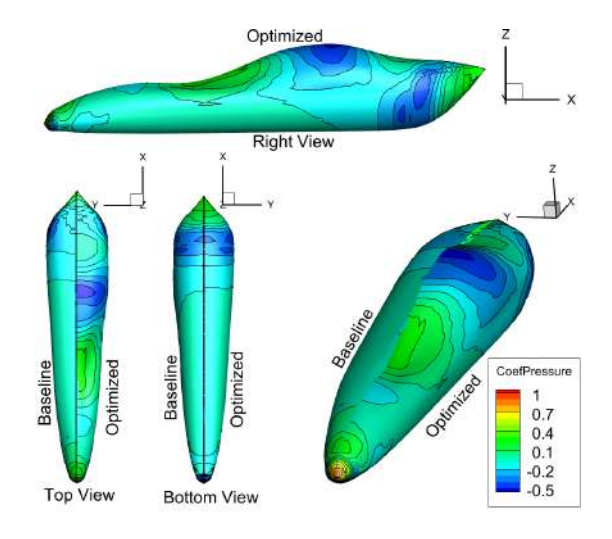


Figure 5: Pressure coefficient distribution on the optimized TEKEVER ARX fuselage of case 3

As observed in the pressure distribution shown in Fig. 5, the optimized fuselage exhibits a completely different pressure distribution when compared to the baseline fuselage. Near the nose, the pressure is still relatively high, as no shape changes in this region were allowed. As flow progresses, the fuse-

Table 2: ARX fuselage aerodynamic shape optimization parameters – Symmetry-Enforced Cases

Variable	Description	Quantity/ Value	
		Case 3	Case 4
Minimize:			
C_D	Drag at fixed flight condition		_
By varying:			
shape_vertical_func	FFD vertical deformations (Y, Z)	30	27
shape_horizontal_func	FFD horizontal deformations	24	18
Subject to:			
x_{FFDy}	Bounds for Y displacements	[-0.1, 0.1]	[-0.1, 0.1]
x_{FFDz}	Bounds for Z displacements	[-0.2, 0.2]	[-0.3, 0.3]
$KS_{\mathrm{geom}} \leq 0$	Aggregated minimum distance (spatial feasibility Condition 1)	1	1
L = 0	Non-intersection (spatial feasibility Condition 2)	1	1
Objective scaling	Scaling factor for objective	500	100
At condition:			
Symmetry	Enforced at $y = 0$	_	

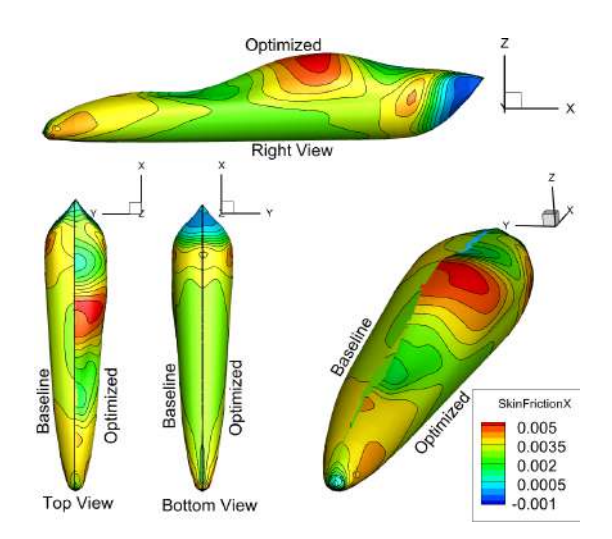


Figure 6: Skin friction coefficient distribution on the optimized TEKEVER ARX fuselage (case 3).

lage begins to widen, causing the flow to decelerate. This results in a local increase in pressure and, consequently, in the pressure coefficient. Near the aft of the fuselage, and once the sphere is fully enclosed, the geometry transitions into a region of decreasing cross-sectional area. This leads to an acceleration of the flow. This behaviour is reflected in the pressure distribution, where a lower pressure region (dark blue) emerges. Near the trailing edge, the geometry appears to provide a relatively smooth pressure recovery, helping to stabilize the flow and reduce potential flow separation.

The skin friction coefficient distribution shown in Fig. 6 complements the pressure data by highlighting the skin-friction patterns. Near the nose, skin friction is low, consistent with the stagnation zone where tangential velocity is minimal. Along the mid-fuselage, skin friction increases steadily, reflecting an attached boundary layer. The highest values are concentrated over the top of the fuselage, particularly around regions of increased curvature where flow speeds are greatest. Towards the tail, C_f gradually decreases, and isolated blue regions, indicating negative or near-zero skin friction, emerge, which may indicates possible flow separations, supporting what was previously discussed.

Overall, the (C_p) and (C_f) distributions give a good indication of how the flow behaves around the optimized fuselage. According to Tab. 3, this final case resulted in a 4.6% reduction in overall drag. In this optimization case (case 3), pressure drag was reduced by around 10.3%, while skin-friction drag increased by approximately 2.3%. This means that the optimizer was able to reduce the total drag by essentially decreasing pressure drag. On the other hand, the increase in skin-friction drag was due to the larger volume and surface area of the fuselage required to enclose the entire sphere, which naturally leads to higher shear forces along the surface.

As already referred, some modifications were made to case 4 to prevent previous issues encountered. To increase the flexibility of the optimizer, while complying with the constraints, and prevent the values of the design variable from reaching the upper boundaries, the upper limits of the applied design variables were increased. This allowed for larger geometric deformations and improved the optimizer ability to adapt the fuselage shape around the box.

Furthermore, the spatial fitness value of the tri-

angulated surface, ρ , was reduced. This parameter controls how close the optimizer is required to match the reference surface, in this case, the box. Reducing ρ helps relax this constraint, giving the optimizer more freedom to prioritize smoother shapes over exact surface matching [19]. The goal was to make the integration of the inclined box easier by avoiding sharp transitions and giving the optimizer more flexibility to generate a continuous fuselage without being forced to fit the triangulated surface too tightly. The optimized fuselage enclosed the entire box while ending in a smooth way, avoiding large pressure coefficient differences and helping to keep the flow attached to the fuselage surface. This, together with the smoothing of the box, allowed a converged solution that respected the constraints.

A detailed comparison between the baseline (left-side) and the optimized fuselage (right-side) for the last case (Case 4) is shown in Figs. 7 and 9. The same methodology is used to demonstrate the distribution of pressure and friction on the fuselages, where a symmetry plane at y=0 is used to divide the different views.

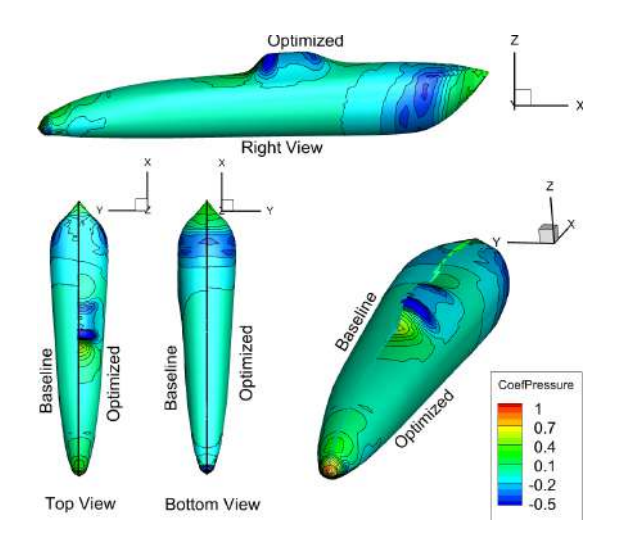


Figure 7: Pressure coefficient distribution on the optimized TEKEVER ARX fuselage (case 4).

As expected, the resulting fuselage is much more similar to the baseline compared to the other cases. This is due to the more restricted displacements applied to the FFD box. However, because the box had to be fully enclosed while avoiding large deformations in the front section of the fuselage, the geometry transitions sharply to enclose the parachute box. This leads to a nearly perpendicular slope in that region, which creates a high-pressure area. Since the box is enclosed, the fuselage experiences a pronounced pressure drop, accelerating the flow around this section. To help maintain flow attachment, a smooth and gradual slope is introduced

in the aft part of the fuselage, following the cross-sectional enlargement.

Nevertheless, as shown in Tab.3, a flow separation occurred due to the significant increase in pressure drag. Specifically, the fuselage experienced an increase of nearly 43% compared to the baseline. Figure 8 illustrates the region where this separation takes place, clearly showing where the streamlines reverse direction, and providing valuable insight into the aerodynamic behaviour of the optimized geometry.

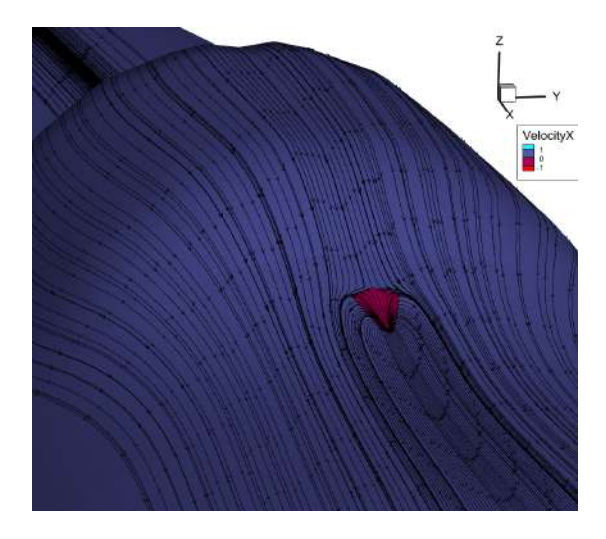


Figure 8: TEKEVER ARX fuselage optimization problem with an integrated box (case 4).

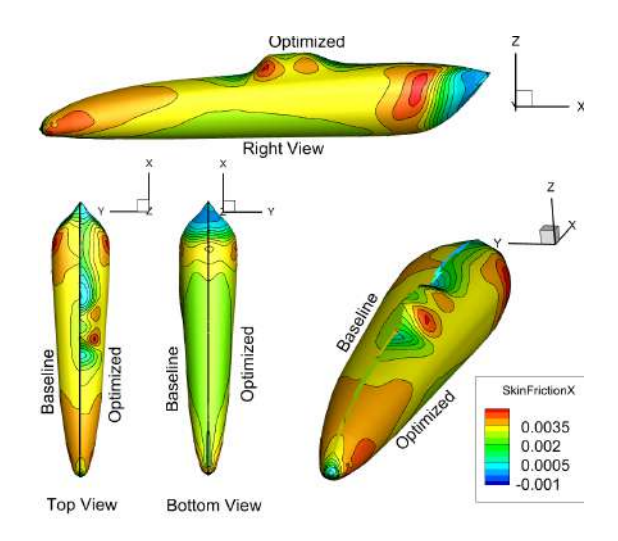


Figure 9: Skin friction coefficient distribution on the optimized TEKEVER ARX fuselage of case 4

The skin friction distribution of the optimized fuselage is compared with the baseline in Fig. 9. As expected, since the fuselage did not undergo any deformations near the nose, it remains identical to that of the baseline in this region. As the flow encounters the wall enclosing the box, the velocity

decreases, and consequently, so does the skin friction. This is visible in the light blue/green region, corresponding to the region where the fuselage cross section begins to expand. Supporting the previous analysis, a second light blue/green region appears where the cross section starts to decrease. In this region however, the velocity does not show a similar reduction, which may indicate a possible flow separation.

Table 3: Comparison of drag coefficient variations and computational time.

Config.	t (h)	ΔC_D	ΔC_{D_p}	ΔC_{D_v}
Baseline	_	Ref	Ref	Ref
Case 3	118	-4.6%	-10.3%	+2.3%
Case 4	121	+24.7%	+42.8%	+2.5%

Overall, several conclusions can be drawn from the analysis of this last case (Case 4). Firstly, it must be noted that, contrary the trends observed in the previous cases, the optimizer was not able to minimize the total drag coefficient (C_D) . This may be attributed to the restrictions applied, as well as the bounds used for the different design variables, which limited the optimizer's flexibility. In Case 4, an increase of approximately 25% in total drag was observed, as shown in Tab. 3. While the skin friction drag increased by only 2.5%, remaining within the range of the increases seen in the previous cases, the pressure drag component rose around 43%. This significant rise in pressure drag is likely due to the nearly perpendicular slope introduced to enclose the box, which created adverse pressure gradients and led to flow separation. This highlights how the smoothness of the fuselage streamlines contribute to flow attachment and, consequently, improve its aerodynamic characteristics.

5. Conclusions

This work used the MACH-Aero framework to perform aerodynamic fuselage shape optimization with payload integration. The objective was to minimize the overall drag while operating under geometric constraints and different design variables. The Free-Form Deformation (FFD) method was used to parametrize the geometry allowing flexible shape control throughout the optimization process.

Several deformation approaches were explored, combined with the triangulated surface constraint method, to ensure that internal payloads could be enclosed without generating infeasible fuselage geometry or compromising flow quality. These approaches were benchmarked using a basic fuselage to establish the limitations and advantages of each, and were used as the foundation to address more realistic cases.

The final optimization cases (Cases 1, 2 and 3)

demonstrated how the integration of these tools and approaches could lead to aerodynamic improvements. In the spheric SATCOM integration case, a total drag reduction of 4.6% was achieved, primarily due to a 10.3% decrease in pressure drag. This gain was slightly offset by an increase of approximately 2.3% in skin-friction drag, caused by the additional surface area required to house the payload. On the other hand, Case 4 presented a different outcome. Despite following the same optimization framework, the stricter design constraints and reduced geometric flexibility led to a total drag increase of approximately 25%. While the increase in skin-friction drag remained within the same range at 2.5\%, the pressure drag rose significantly, by about 43%, highlighting the adverse effects of the abrupt fuselage expansion required to enclose the payload.

It is important to note that, compared to the first studies, these final optimization problems were subject to stricter constraints. Since the geometry aimed to represent a real-case scenario, changes to the fuselage could potentially affect the positioning of internal components or structural elements. These restrictions limited the design space available to the optimizer but made the problem more realistic. Despite this, the results showed that even under such limitations, several aerodynamic gains can still be achieved. This reinforces the potential of the adopted optimization framework to support and help improving future geometries, taking into account different constraints and design variables.

Overall, this work provided valuable insights regarding aerodynamic shape optimization of fuse-lages. It contributed to a deeper understanding on how to parametrize different geometries, taking into account the several risks and irregularities that might be obtained if the problem is not properly defined. It also provided knowledge in constraint enforcement, particularly regarding the triangulated surface constraint method, and how these approaches can be combined to produce the best possible solution for enclosing various payloads into the fuselage.

References

- B. Naveen K Karthik Reddy, SK. Kamil Basha and K. Abhilash. The game-changing role of drones in agriculture. Agri Express, 02, may 2024. ISSN 2584 - 2498.
- [2] Ö. Ö Kanat. The significance of unmanned aerial vehicles (UAVs) in strategic contexts. *Anadolu Strateji Dergisi*, 5(2):75–87, 2023.
- [3] G. K.W. Kenway, C. A. Mader, P. He, and J. R. R. A. Martins. Effective adjoint approaches for computational fluid dynamics. *Progress in Aerospace Sciences*, 110:100542, 2019. ISSN 0376-0421. doi:10.1016/j.paerosci.2019.05.002.
- [4] J. Reid and P. He. Free-Form Deformation (FFD). DAFoam, February 2021. URL https://dafoam.github.io/docs/FFD/ main.pdf. Accessed on May 25, 2025.
- [5] J. Anderson. Fundamentals of Aerodynamics. McGraw-Hill series in aeronautical and aerospace engineering. McGraw-Hill Education, 6 edition, 2017. ISBN 978-1-259-12991-9.
- [6] Snorri Gudmundsson. Chapter 16 aircraft drag analysis. In Snorri Gudmundsson, editor, General Aviation Aircraft Design, pages 657–752. Butterworth-Heinemann, second edition edition, 2022. ISBN 978-0-12-818465-3. doi:10.1016/B978-0-12-818465-3.00016-1.
- [7] P. K. Kundu, I. M. Cohen, and D. R. Dowling, editors. Fluid Mechanics. Academic Press, fifth edition edition, 2012. ISBN 978-0-12-382100-3. doi:10.1016/C2009-0-63410-3.
- [8] E.L. Houghton, P.W. Carpenter, Steven H. Collicott, and Daniel T. Valentine. Chapter 8: [viscous flow and boundary layers]. In Aerodynamics for Engineering Students. Butterworth-Heinemann, Oxford, UK, 6 edition, 2012. ISBN 978-0-08-096632-8.
- [9] P.R Spalart. Strategies for turbulence modelling and simulations. *International Journal of Heat and Fluid Flow*, 21(3):252–263, 2000. doi:10.1016/S0142-727X(00)00007-2.
- [10] N. Azwadi C. Sidik, S. Nurul Akmal Yusof, Y. Asako, S. Mohamed, and A. Aziz. A short review on RANS turbulence models. *CFD Letters*, 12:83–96, 11 2020. doi:10.37934/cfdl.12.11.8396.
- [11] C. A. Mader, G. K. W. Kenway, A. Yildirim, and J. R. R. A. Martins. ADflow—an open-source computational fluid dynamics solver for

- aerodynamic and multidisciplinary optimization. *Journal of Aerospace Information Systems*, 2020. doi:10.2514/1.I010796.
- [12] J. R.R.A. Martins and Andrew Ning. Engineering design optimization. Cambridge University Press, 2021. ISBN 9781108833417.
- [13] Y. Ma, X. Gao, C. Liu, and J. Li. Improved SQP and SLSQP algorithms for feasible path-based process optimisation. *Computers & Chemical Engineering*, 188:108751, 2024. doi:10.1016/j.compchemeng.2024.108751.
- [14] University of Michigan MDO Lab. MACH-aero framework. https://github.com/mdolab, 2023. Accessed: May 2025.
- [15] N. R. Secco, G. K. W. Kenway, P. He, C. Mader, and J. R. R. A. Martins. Efficient mesh generation and deformation for aerodynamic shape optimization. *AIAA Journal*, 59 (4):1151–1168, 2021. doi:10.2514/1.J059491.
- [16] E. Wu, G. Kenway, C. A. Mader, J. Jasa, and J. R. R. A. Martins. pyoptsparse: A python framework for large-scale constrained nonlinear optimization of sparse systems. *Jour*nal of Open Source Software, 5(54):2564, 2020. doi:10.21105/joss.02564.
- [17] J. Blazek. Computational Fluid Dynamics: Principles and Applications. Elsevier, 3rd edition, 2015. ISBN 9780080999951.
- [18] G. K. W. Kenway, N. Secco, J. R. R. A. Martins, A. Mishra, and K. Duraisamy. An efficient parallel overset method for aerodynamic shape optimization. In 58th AIAA/ASCE/AHS/ASC Structures, Structural Dynamics, and Materials Conference, Grapevine, TX, 2017. doi:10.2514/6.2017-0357.
- [19] B. J. Brelje, J. L. Anibal, Anil Yildirim, C. A. Mader, and J. R. R. A. Martins. Flexible formulation of spatial integration constraints in aerodynamic shape optimization. AIAA Journal, 58(6):2571–2580, 2020. doi:10.2514/1.J058366.